Science Advances
AAAS

advances.sciencemag.org/cgi/content/full/7/10/eabf0452/DC1

Supplementary Materials for

On secondary atomization and blockage of surrogate cough droplets in single- and multilayer face masks

Shubham Sharma, Roven Pinto, Abhishek Saha, Swetaprovo Chaudhuri, Saptarshi Basu*

*Corresponding author. Email: sbasu@iisc.ac.in

Published 5 March 2021, *Sci. Adv.* **7**, eabf0452 (2021)
DOI: 10.1126/sciadv.abf0452

The PDF file includes:

Figs. S1 to S10

Other Supplementary Material for this manuscript includes the following:

(available at advances.sciencemag.org/cgi/content/full/7/10/eabf0452/DC1)

Movies S1 to S5

Supplementary figures

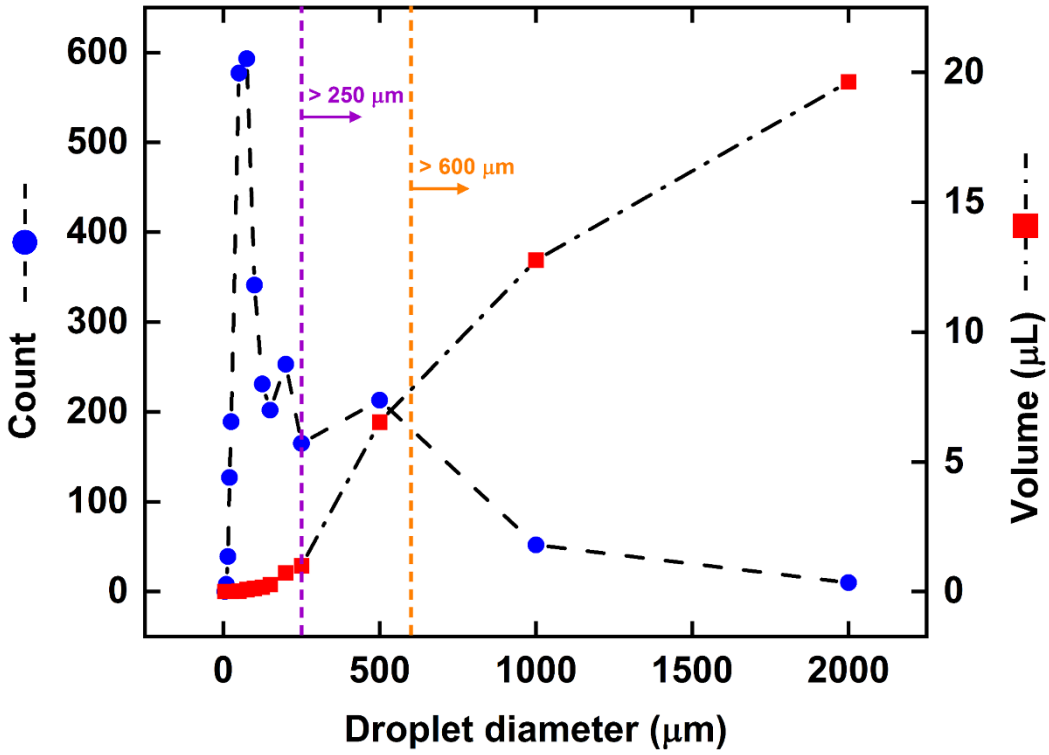

Supplementary Fig. S1. Size and volume distribution of droplets expelled during coughing. The size distribution is as given in Duguid (1946) for measurement involving 3000 droplets, ejected during 10 – 22 expiratory events. Two vertical lines with arrows are used to indicate the sizes greater than 250 μm and 600 μm**.** Volume percentage of droplets with diameter greater than 250 μm is 94.21%, and greater than 600 μm is 72.22%.

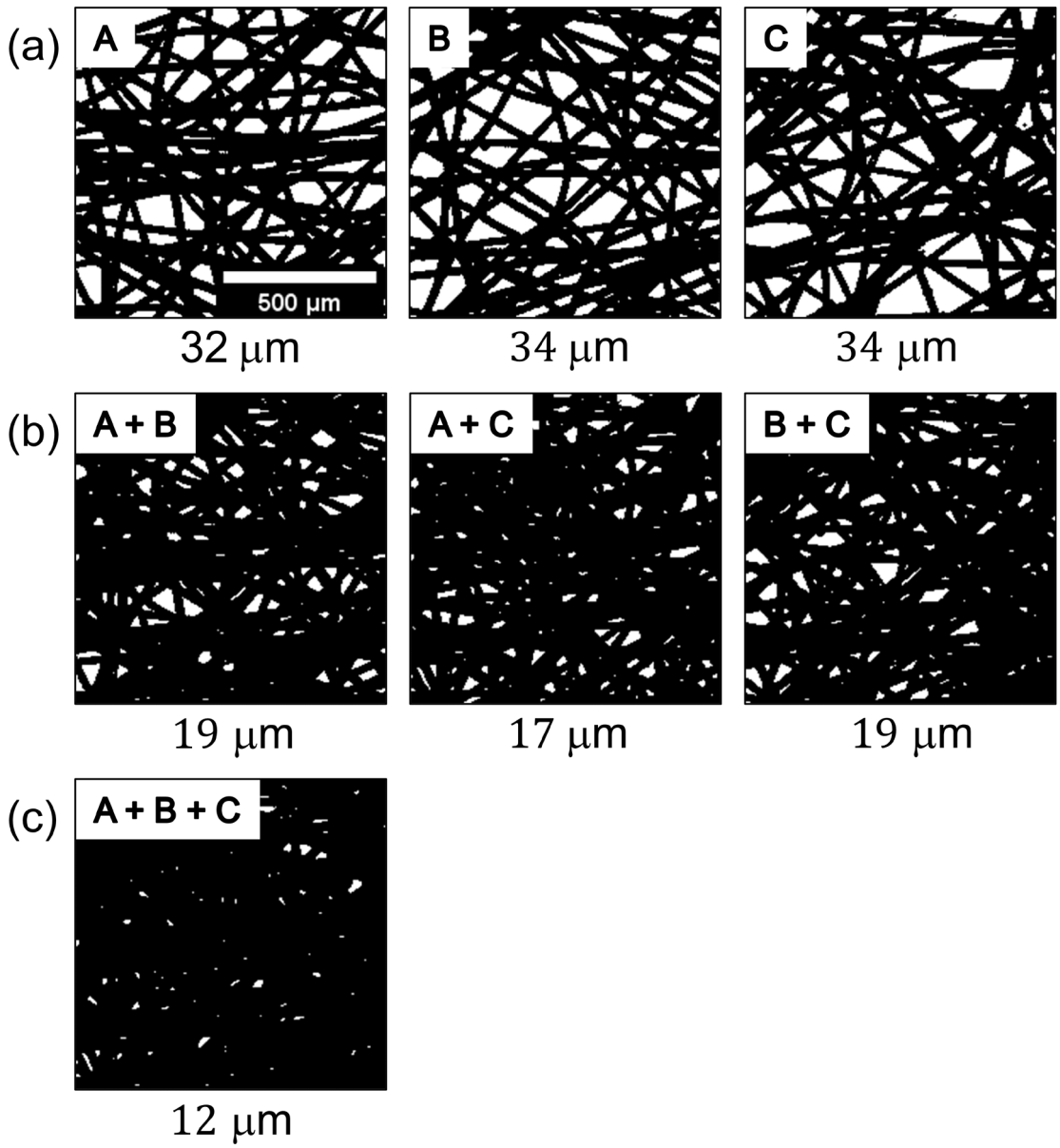

Supplementary Fig. S2. Measurements of pore size for masks with different number of layers. (a) Microscopy image of single-layer mask. Pore sizes are directly obtained from the pore areas measured using the ImageJ software, and average effective diameter was found to be of 30 μm. (b - c) Overlayed images formed by merging two and three single-layer microscopy images to form double- and triple-layers, respectively. Pore sizes are obtained by calculating the pore areas from these images, and the average effective diameter was found to be of 17 μm and 12 μm for double- and triple-layer masks, respectively. Scale bar is described in the figure.

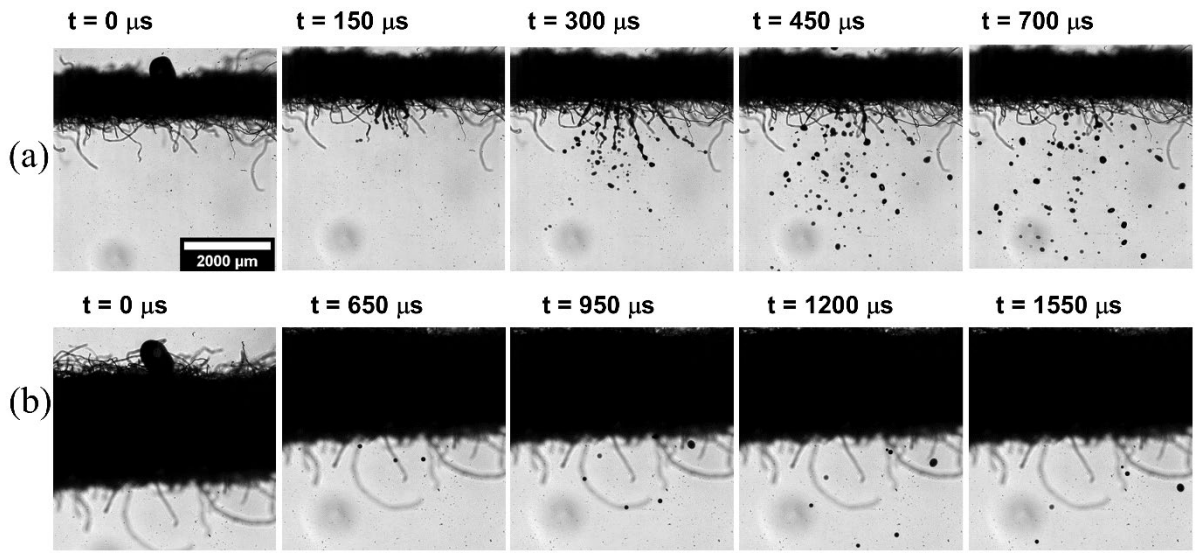

Supplementary Fig. S3. Dynamic images of a droplet impacting on different layered cloth mask. The water droplet impacting on the mask surface has a "*We* ~ 880" and is recorded at 20000 fps. (a - b) Time sequence images of droplet impingement on a single- and double-layer of cloth mask respectively. The total number count of atomized droplets is significantly higher for the single-layer mask in comparison with the double-layer mask. Bush like structure observed in the images are the threads used for making the mask and are unavoidable during experiments. Scale bar description is included in the figure.

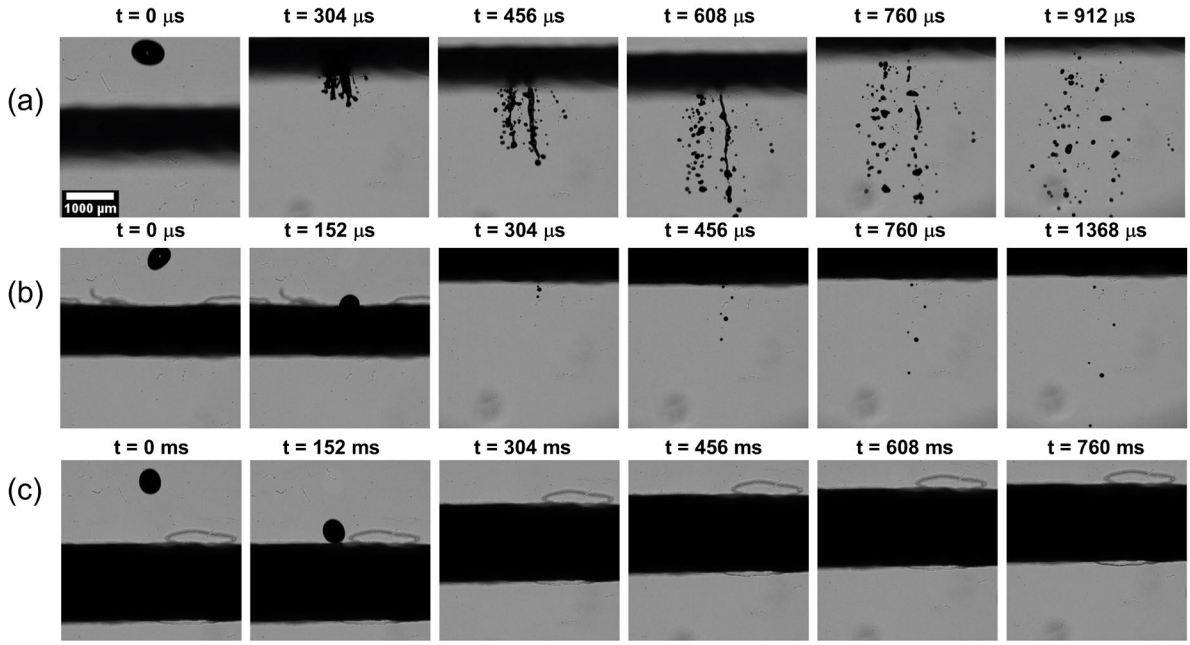

Supplementary Fig. S4. Dynamic images of a droplet impacting on different layered mask B. The water droplet impacting on the mask surface has a "*We* ~ 880" and is recorded at 20000 fps. (a - c) Time sequence images of droplet impingement on a single-, double-, and triple-layer mask, respectively. The total number count of atomized droplets is significantly higher for the single-layer mask in comparison with the double-layer mask, while no droplet penetrates through the triple-layer mask (see Fig. 2(c) at "t = 152 - 760 μs"). Scale bar description is included in the figure.

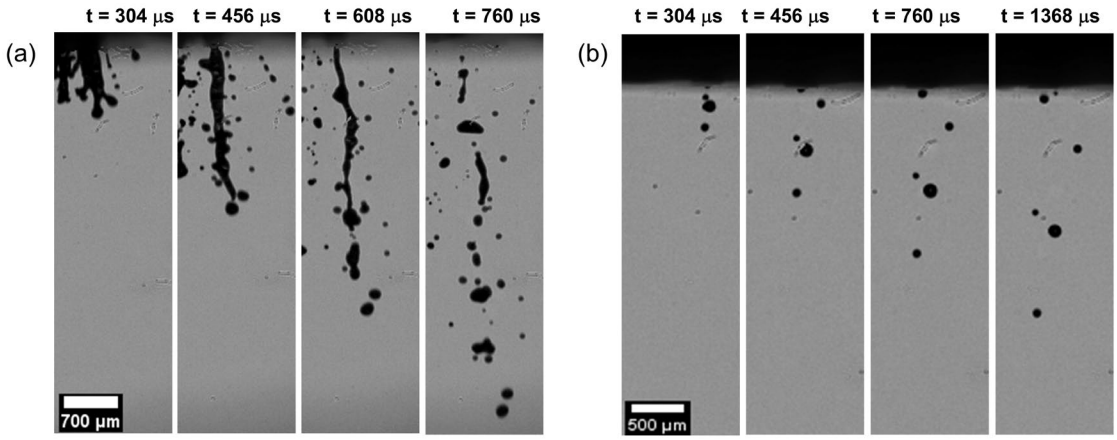

Supplementary Fig. S5. Cropped images of droplet atomization through mask B. (a) Impingement on a single layer of mask B is recorded at 6200 fps and "*We* ~ 880". The impacting droplet extrudes through the mask layer as a cylindrical ligament "(t = 304 μs)" whose length increases over time "(t = 304 – 456 μs)". Unstable waves are formed on the surface of the ligament, which grows in amplitude "(t = 456 – 608 μs)" and leads to its atomization into tiny droplets "(t = 760 μs)" via the Rayleigh plateau instability. (b) Impingement on a double-layer mask. The total number count of the daughter droplets is significantly less, and no ligament formation is observed "(t = 304 – 1368 μs)". Scale bar description is included in the figures.

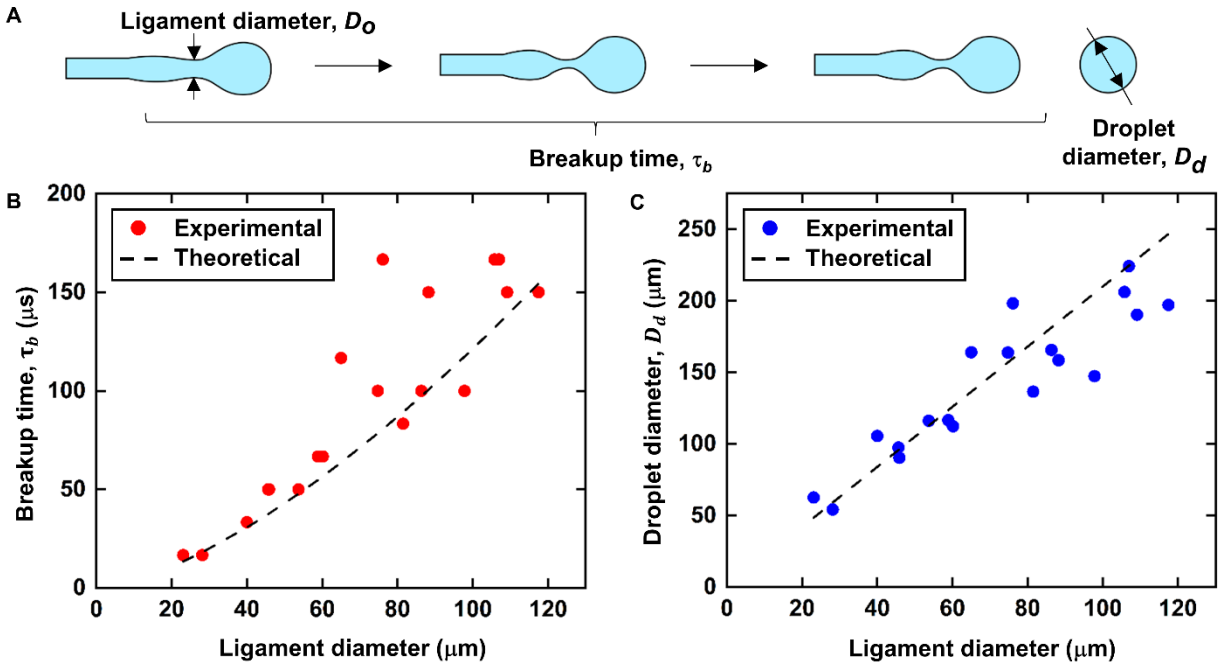

Supplementary Fig. 6. Breakup time and daughter droplet diameters. (**A**) Schematic diagram displaying different stages of a ligament undergoing breakup via Rayleigh-Plateau instability. (**B, C**) Comparison of experimental and theoretical breakup times and daughter droplet diameters for different ligament sizes.

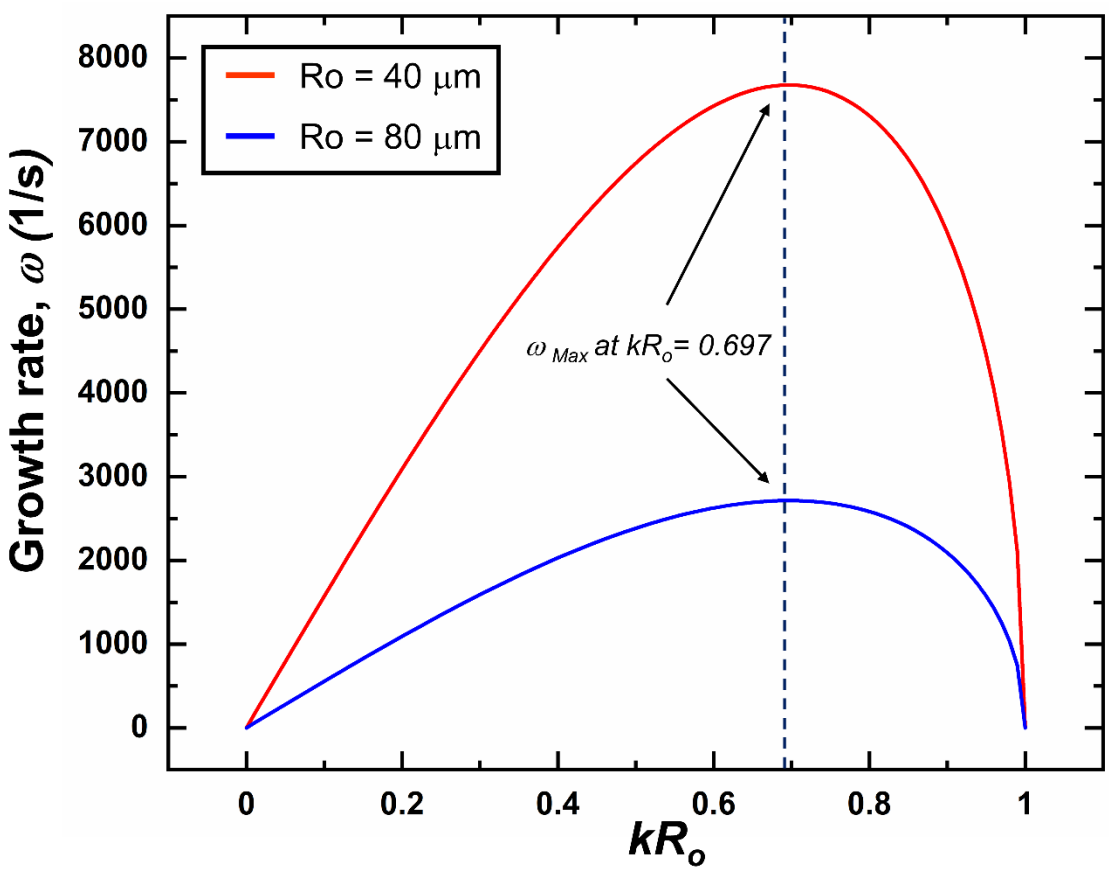

Supplementary Fig. S7. Growth rate of instabilities in Rayleigh-Plateau breakup. The growth rate of instability at "$0 < kR_o < 1$" for ligament thicknesses of 40 μm and 80 μm. Maximum growth rate which leads to ligament breakup occurs at "$kR_o = 0.697$".

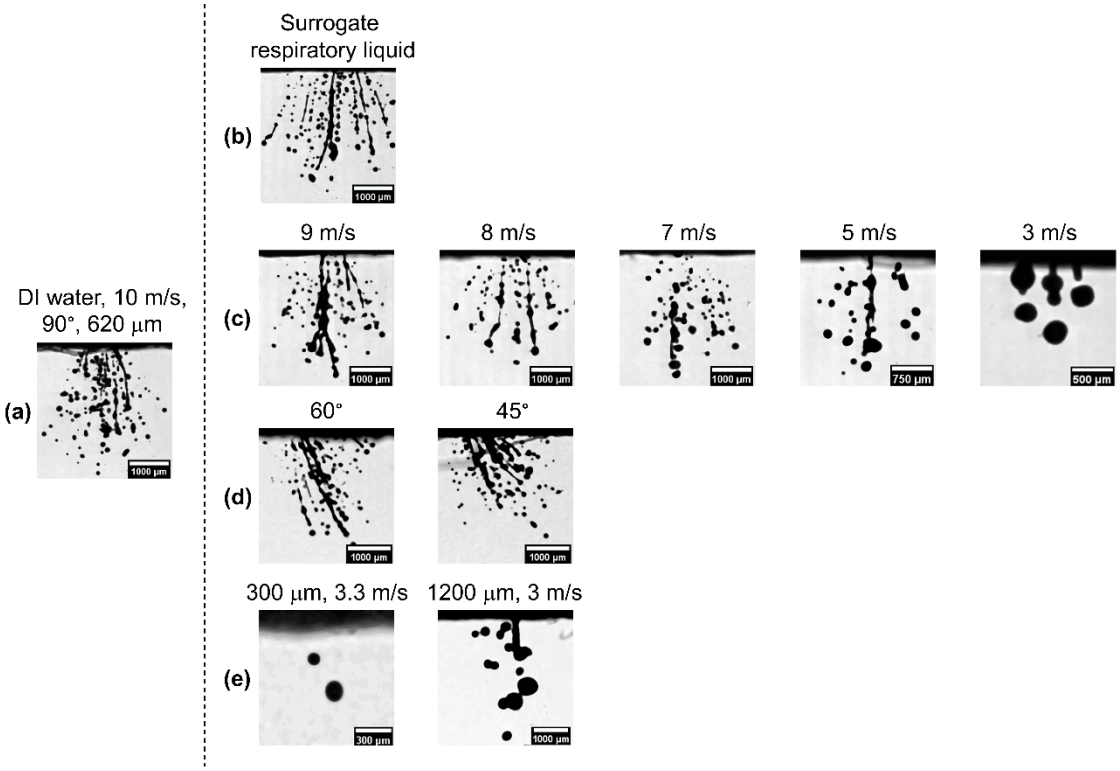

Supplementary Fig. S8. Fragmentation images of different experimental cases for single-layer mask B. (a) Primary case (b) Surrogate respiratory fluid (c) Different velocities of impact (d) Different angles of impingement (e) Small and large-sized droplets impacting at near penetration threshold velocity. Scale bars are included in the figures.

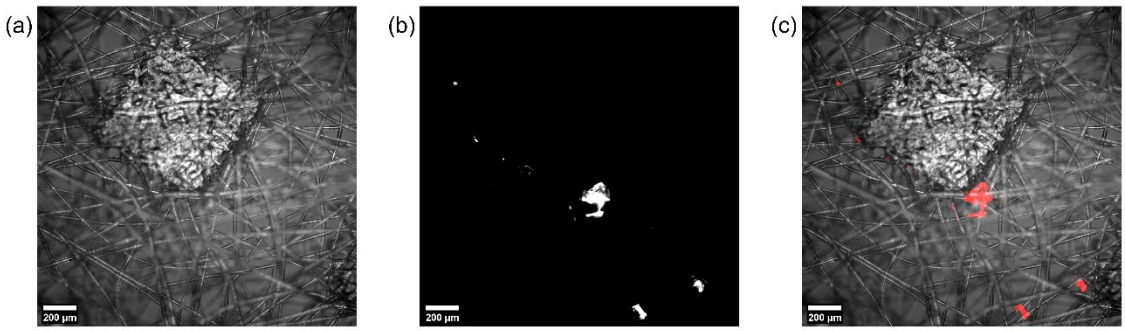

Supplementary Fig. S9. Procedure for image overlaying. (a) Bright-field image of mask layer. (b) Corresponding fluorescent image. (c) Overlayed image formed as a colour image by merging the bright-field image on grey channel and fluorescent image on the red channel.

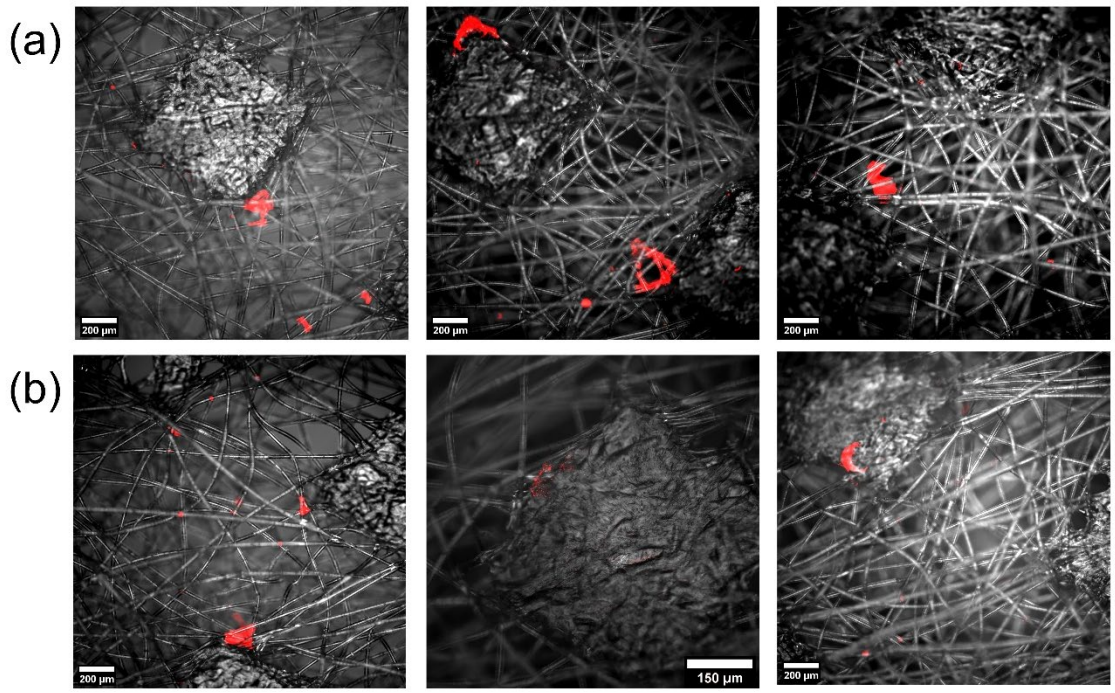

Supplementary Fig. S10. Viral load trapping on mask B. (a) Overlayed bright-field and fluorescent microscopy images showing trapped particles on the impact side for a single-, double-, and triple-layer of mask B (left to right in order). (b) Overlayed bright-field and fluorescent microscopy images shows the trapped particles on the penetration side for a single-, double-, and triple-layer of mask B (left to right in order). Scale bar description is included in the figures.